

Energy assessment for integration of concrete thermal energy storage with low-grade solar power generation system

Amin Shakeri^a, Hossein Eshghi^b, Farhad Salek^c, Meisam Babaie^{d,*}

^a Department of Mechanical, Industrial, and Aerospace Engineering, Concordia University, Montreal, Quebec, H3G 2W1, Canada

^b Faculty of Mechanical and Mechatronic Engineering, Shahrood University of Technology, Shahrood, Iran

^c Faculty of Technology, Design and Environment, Oxford Brookes University, OX3 0BP, Oxford, UK

^d School of Mechanical Engineering, University of Leeds, LS2 9JT, Leeds, UK

ARTICLE INFO

Keywords:

Thermal energy storage
Organic rankine cycle
Concrete
Compound parabolic collector
District heating

ABSTRACT

The energy storage systems are one of the essential components of the renewable energy systems to manage the energy supply and demand. The integration of a novel concrete thermal energy storage system with solar-driven organic Rankine cycle is studied in this paper. The Compound Parabolic Collectors (CPC) are used for absorption of solar energy. The solar energy is then transferred to Thermal Energy Storage (TES) and Organic Rankine Cycle (ORC) for heat storage and power generation. For evaluating the performance of proposed system, it is modeled numerically, and a parametric study is performed to find the optimum parameters of TES for maximizing the ORC working hour period. The results show that the increase in TES pipe length leads to an increase in TES charging time and heat capacity up to 82 h and 660 kW with 1000 m² solar panel surface. Furthermore, the ORC working hours is extended by 3:10 h in a day by using the optimized TES concrete section with the length of 2000 m and diameter of 0.4 m. Additionally, the employment of TES in solar-driven ORC system resulted in the reduction of system power generation by 1.3% and an increment of heat generation by 0.49%.

1. Introduction

The greenhouse gas emissions originated from powerplants in which the fossil fuel is burnt for electrical power generation impose lots of negative impacts on the environment [1]. Accordingly, different government bodies and research organizations are looking for alternative and sustainable energy systems which can be employed for power generation instead of existing thermal powerplants [2,3].

One of the efficient methods for sustainable electrical power generation is the integration of novel thermal cycles such as Organic Rankine cycle [4] and Kalina cycle [5] with solar thermal collectors. In such systems, the thermal energy absorbed by the thermal collectors will be transferred to the proposed thermal cycle via a heat exchanger [6]. However, one of the main challenges of such solar-driven energy systems is the fluctuations in electrical energy generation rate at various times of the day [7,8]. For the integrated configuration, electrical energy generation by the thermal cycle starts at the sunrise, then increases at noon because the maximum solar radiation is available for the collectors, and it decreases to zero until the sunset.

The energy storage systems can be employed to rectify the electrical

power generated by the solar-driven thermal cycles [8]. Various energy storage systems with different mechanisms were suggested to increase the effectiveness of solar-driven power generation systems, such as chemical batteries, pumped-storage hydropower, compressed air energy storage, and thermal energy storage systems [9]. Integration of the TES with solar power generation technologies results in providing electrical power for longer time during off-peak hours as well as peak hours [8, 10]. Besides electric generation by the CPC system, the low-temperature HTF can be used for district heating. The district heating demand is usually higher in the afternoon, so using a TES system can be a solution for providing solar heating energy continuously [11,12]. In this concept, Leško et al. [13] optimized a system with CHP and TES for district heating usage and recommended a financially efficient operating condition. Also, Zhang et al. [14] compared four different TES systems to find the most efficient system to be used in domestic heating. In a more comprehensive study, Xi et al. [15] accomplished energy, exergy, and exergoeconomic analysis of a solar system integrated with TES for power and freshwater generation.

Historically, the phase change material (PCM) storage systems are commercialized and used to store solar thermal energy in solar energy systems [16]. However, there are many challenges in using PCM storage

* Corresponding author.

E-mail address: M.Babaie@leeds.ac.uk (M. Babaie).

<https://doi.org/10.1016/j.renene.2023.119249>

Received 5 December 2022; Received in revised form 2 August 2023; Accepted 29 August 2023

Available online 30 August 2023

0960-1481/© 2023 The Authors. Published by Elsevier Ltd. This is an open access article under the CC BY license (<http://creativecommons.org/licenses/by/4.0/>).

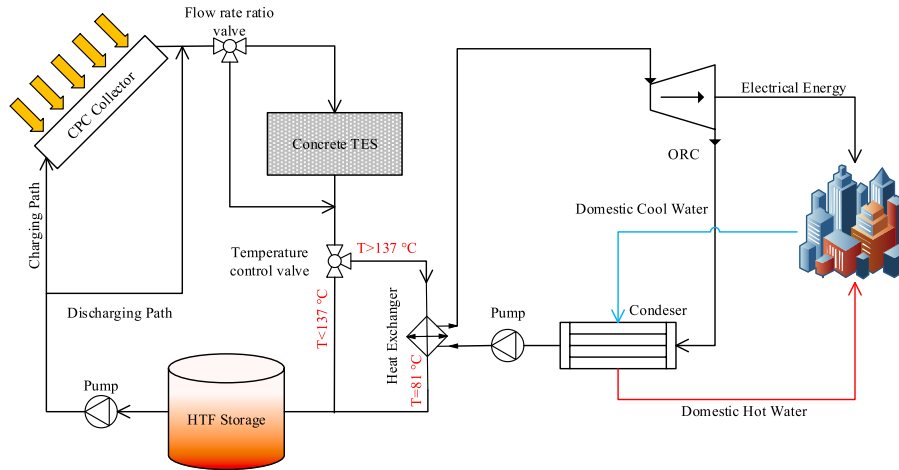


Fig. 1. The block diagram of the proposed system.

After the expansion of ORC working fluid in the turbine, it flows through a condenser in which it will be cooled down until it condenses. The cooling down process in the condenser leads to rejection of heat to coolant water and increases its temperature. Therefore, hot water can also be produced and used for district heating requirements. For the simulation of this system, a 1000 m² solar panel has been assumed for this study and the length and diameter of the TES system are optimized for the best performance and durability.

3. Mathematical modeling

Each component shown in Fig. 1 is considered as a control volume, and the first law of thermodynamics is applied to perform energy analysis for the proposed system [30,31]. The main equations applied to each control volume can be listed as follows [31]:

- Mass equation:

$$\sum \dot{m}_i = \sum \dot{m}_e \quad (1)$$

- Energy equation:

$$\sum \dot{Q} + \sum \dot{W} = \sum \dot{m}_e h_e - \sum \dot{m}_i h_i \quad (2)$$

The following assumptions are overall assumptions made for the mathematical modeling of the system [30]:

- Pressure-drop due to friction in pipes is neglected
- The LMTD method is employed for the calculation of the heat transfer in the heat exchangers

3.1. Compound parabolic collector

In the mathematical modeling process of the compound parabolic collectors, the absorbed solar irradiation per unit area of the collector is obtained by Ref. [32]:

$$S = G_{CPCB} \tau_{cB} \tau_{CPCB} \alpha_B + G_{CPCD} \tau_{cD} \tau_{CPCD} \alpha_D + G_{CPCG} \tau_{cG} \tau_{CPCG} \alpha_G \quad (3)$$

where G_{CPC} , τ_c , τ_{CPC} and α are solar radiation, the transmittance of the CPC cover, the transmissivity of CPC, which accounts for reflection loss and absorptance of the receiver, consecutively. The calculation of aperture area and the useful energy absorbed by the CPC collector is obtained from Equations (4) and (5) [32]:

$$C = \frac{A_a}{A_r} \quad (4)$$

$$Q_u = F_R [S A_a - A_r U_L (T_i - T_a)] n_{col} n_{row} \quad (5)$$

where Q_u , F_R , S , A_a , A_r , U_L , T_i and T_a are absorbed useful energy, heat removal factor, absorbed radiation, aperture area, receiver area, heat loss coefficient, the fluid temperature at the inlet, and ambient temperature, respectively. Moreover, the n_{row} and n_{col} are the number of CPC in rows and columns in the solar field, respectively. The heat loss coefficient and the heat removal factor can be defined by Ref. [32]:

$$U_L = \left[\frac{A_r}{(h_w + h_{re\ c-a}) A_c} + \frac{1}{h_{re\ r-c}} \right]^{-1} \quad (6)$$

$$h_w = \frac{Nu K}{D_c} \quad (7)$$

$$h_{re\ r-c} = \frac{\sigma (T_r^2 + T_c^2) (T_r + T_c)}{\frac{1}{\epsilon_r} + \frac{A_r}{A_c} \left(\frac{1}{\epsilon_c} - 1 \right)} \quad (8)$$

$$h_{re\ c-a} = \epsilon_c \delta (T_c + T_{amb}) (T_c^2 + T_{amb}^2) \quad (9)$$

$$F_R = \frac{\dot{m} c_p}{A_a U_L} \left[1 - \exp \left(- \frac{U_L F A_a}{\dot{m} c_p} \right) \right] \quad (10)$$

$$F = \frac{1/U_L}{\frac{1}{U_L} + \frac{D_a}{h_f D_i} + \left(\frac{D_a}{2k} \ln \frac{D_o}{D_i} \right)} \quad (11)$$

where \dot{m} and c_p are mass flow rate and specific heat of CPC working fluid, respectively. The rate of energy loss in the HTF storage tank is given by Ref. [32]:

$$Q_{tl} = (UA)_s (T_s - T_{amb}) \quad (12)$$

where $(UA)_s$ and T_{amb} are storage tank heat loss coefficient, storage tank area and ambient temperature, consecutively. The new storage tank temperature for the next time step will be calculated using Equation (13) [32]:

$$T_{1-n} = T_1 + \frac{\Delta t}{(Mc_p)_s} [Q_u - Q_l - Q_n] \quad (13)$$

The thermal load, which indicates the amount of heat transferred to ORC, is defined as:

$$Q_l = \dot{m}c_p(T_{S,i} - T_{CPC,o}) \quad (14)$$

Finally, the CPC's overall efficiency is:

$$\eta_{CPC} = \frac{\dot{Q}_u}{G_i A_a} \quad (15)$$

The specifications of the CPCs for the solar thermal energy absorption system is presented in Table A1 in Appendix A.

3.2. The thermal energy storage system

As shown in Fig. 2a, the proposed TES base material is concrete in the center of which a long tube is installed. In practice, the proposed system can be buried under the foundation required for the solar field. Therefore, the sizing of the TES is in direct relation to the dimensions of the solar field in this study.

The long tube is simulated using 2D axis-symmetric conduction model and the control volume for discretization is shown in Fig. 2b. The inside radius (Ri) equals 0.025 m, while the outside radius (Ro) and length (L) of the TES are considered variables in this study. The waste heat from the exterior wall is neglected, and the heat conduction is formulated by using Equation (16) [33]:

$$\frac{1}{r} \frac{\partial}{\partial r} \left(r \frac{\partial T}{\partial r} \right) + \frac{\partial^2 T}{\partial Z^2} = \frac{1}{\alpha} \frac{\partial T}{\partial t} \quad (16)$$

Where the α is the thermal diffusivity and is given by Equation 17 [33]:

The heat transfer between the fluid and the inner wall is calculated using the convection heat transfer equation (Equation (18)) [33]. The pipe is discretized in one dimension, and each discretized element parameter has been solved in various timesteps.

$$q = hA_w(T_w - T_b) \quad (18)$$

where, h is the convection heat transfer coefficient, A_w is the inner surface of the TES pipe, T_w and T_b are the inner surface temperature and fluid bulk temperature, respectively. The heat transfer coefficient is calculated using Equation (19) [33]:

$$h = \frac{Nu_D k_f}{D} \quad (19)$$

where Nu_D is the local Nusselt number for the pipe, k_f is the fluid thermal conductivity and D is the pipe diameter. For having the flow regime to be turbulent for most of the time in the pipes, the pipe diameter is considered to be 5 cm in this study. For fully developed and turbulent flow in a smooth pipe, Nu_D is calculated using the Gnielinski [34] (Equation (20)) correlation which is valid when $0.5 \leq Pr \leq 2000$ and

$$3000 \leq Re_D \leq 5 \times 10^6.$$

$$Nu_D = \frac{(f/8)(Re_D - 1000)Pr}{1 + 12.7(f/8)^{1/2}(Pr^{2/3} - 1)} \quad (20)$$

Where f is the Darcy Friction Factor, Re_D is the Reynolds number for the pipe, and Pr is the Prandtl number. Since the pipe flow regime is turbulent, the f can be calculated using Petukhov [35] correlation as presented by Equation (21).

$$f = (0.790 \ln Re_d - 1.64)^{-2} \quad (21)$$

In addition, Therminol is used as the solar system working fluid, the thermophysical properties of which are obtained from the equations provided in Table A2 in Appendix A.

The error for the iterative method used for simulation of TES is $err < 10^{-4}$ for each time step, then it continues to the next time step till the end of 1 h.

3.3. The organic rankine cycle

For simulation of the ORC power generation system, the first law of thermodynamics is employed and applied to its components as follows [30];

$$\dot{Q}_{HEX} = \dot{m}_{orc}(h_e - h_i) \quad (22)$$

$$\dot{Q}_{Cond} = \dot{m}_{orc}(h_i - h_e) \quad (23)$$

where \dot{m}_{orc} , \dot{Q}_{Cond} and \dot{Q}_{HEX} are ORC working fluid mass flow rate, the rate of heat transferred from ORC condenser to domestic water for district heating and the rate of heat transferred from solar thermal energy absorption system to ORC, respectively. In addition, the ORC turbine and pump power generation and consumption rates can be calculated using Equations (24) and (25) [30]:

$$\dot{W}_t = \dot{m}_{orc}(h_i - h_e) \quad (24)$$

$$\dot{W}_p = \dot{m}_{orc}(h_e - h_i) \quad (25)$$

\dot{W}_t and \dot{W}_p are the ORC's turbine power generation and pump power consumption rates, respectively. The overall electrical power generation rate using ORC can be calculated by Equation (26) [30]:

$$\dot{W}_e = \eta_e \eta_m (\dot{W}_t - \dot{W}_p) \quad (26)$$

where η_e , η_m and \dot{W}_e are electrical efficiency, mechanical efficiency, and electrical power generation rate, consecutively. The constant parameters of the ORC system are presented in Table A3 in Appendix A.

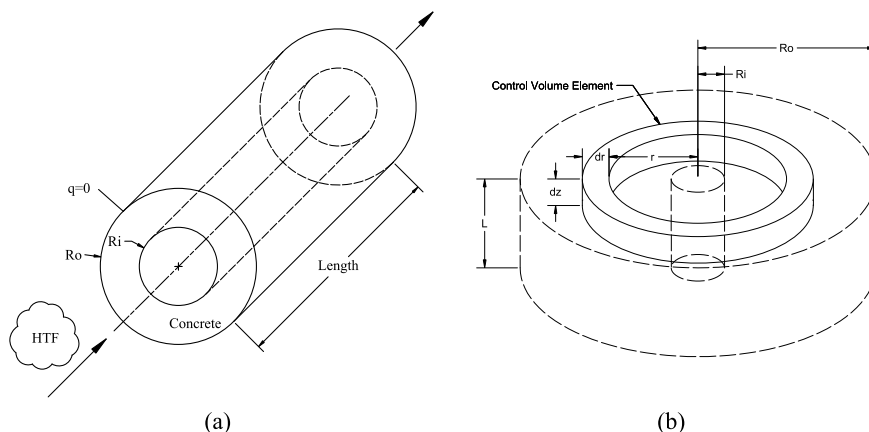


Fig. 2. The schematic diagram of (a) the proposed concrete TES cut section, (b) concrete conduction heat transfer control volume.

3.4. System integration

Fig. 3 shows the calculation flow chart of the present study. After system initialization, the calculation for every time step starts from the CPC system, and the results will go to TES and then ORC systems. After reaching the desired amount of time, the program will be finished.

4. Validation

Two strategies are considered to validate the concrete TES model developed in this study. According to the description presented in the methodology, the TES module is separated into two sections: the pipe where the solar system working fluid flows through and the concrete where the heat will be stored. Each of the models developed for these two sections is validated against the empirical correlations [33].

The flow inside the pipe is validated against the Gnielinski correlation with the LMTD temperature difference for the entire length of the pipe. The wall boundary condition is considered a constant temperature wall. The simulation repeated for different Reynolds numbers and pipe lengths, and the results were validated in each case. For instance, Fig. 4 shows the dimensionless temperature variation along the pipe length. The simulation results presented in Fig. 4 are compared with the standard engineering usage of the correlation (for Gnielinski). Therefore, it can model the heat transfer between the solar system working fluid and the concrete inner wall.

The concrete heat transfer model results are validated against the first law of thermodynamics. In our case, the outer wall is considered an insulated wall, and the inner wall is considered a wall with constant heat flux at various time steps. The amount of stored heat will be calculated from Equation (27) [33], and it will be compared with the amount of conducted heat inside the concrete. The most critical parameter for TES accuracy is the number of nodes in the radial direction. Fig. 5 shows five different outside diameter error trends when the outside diameter of the TES medium increased. By increasing the outside diameter, the error increased significantly. After increasing the number of nodes in the radial direction, the computational load of the model also increases. Therefore, there will be a trade-off between the speed of solving the

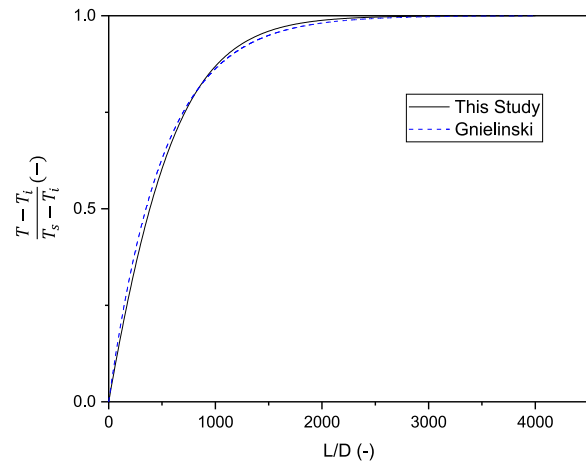


Fig. 4. Comparison of the heat transfer in a simple pipe (Gnielinski versus this study).

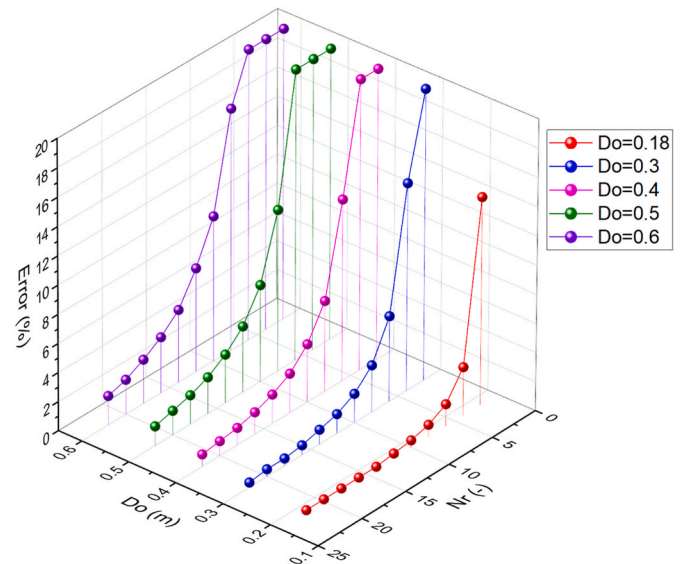


Fig. 5. The TES simulation error in various outer diameters.

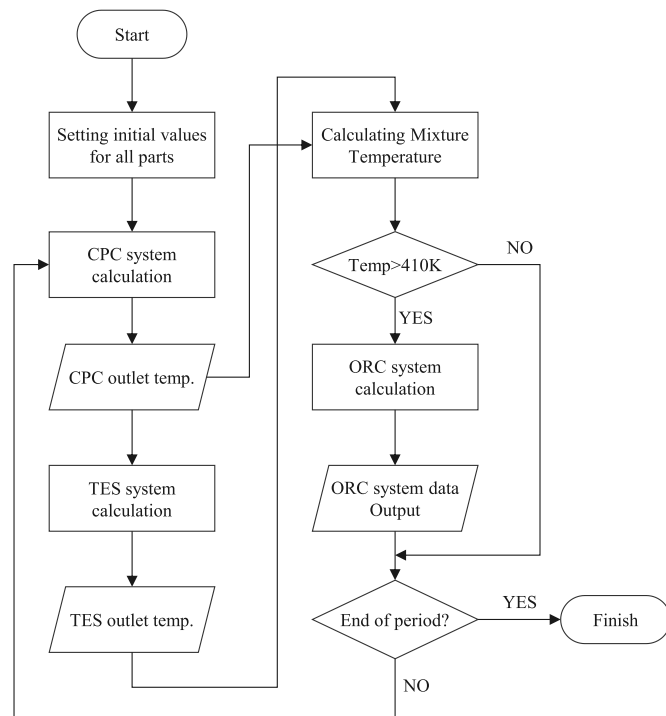


Fig. 3. System calculation flow chart.

model and accuracy. For this study, the number of nodes is set by keeping the maximum error below 2% for all cases.

$$q_s = mC_p(T_{final} - T_{initial}) \quad (27)$$

5. Result and discussion

The solar system is simulated by using the conditions provided in Appendix B.

5.1. TES parametric analysis

To evaluate the impacts of the TES pipe length on the charging and the discharging process, the TES temperature in three different pipe lengths is studied. In the charging process, the initial temperature of 25 °C is considered for the medium (concrete). When the hot fluid flows through the pipe, the charging process begins and continues until the temperature difference between initial and inlet temperature reaches 99%. After that, the discharging process is started when the fluid with the initial TES temperature flows through the pipe. Three main parameters, such as the fluid outlet temperature, mean temperature of the

TES, and the temperature in which the TES reaches 99% charging time (which is an indicator of storage capacity), are presented in Fig. 6 for each pipe length.

Fig. 6a shows the charging and discharging process of the concrete TES system for the pipe with 500 m long and 0.4 m outside diameter. As demonstrated in this figure, during the charging period, the outlet temperature is always higher than the TES mean temperature, and it takes approximately 40 h for TES to be fully charged. Fig. 6b and c indicate that increment of TES pipe length to 1000 m and 2000 m results in an increase of charging time to 56 h and 82 h, respectively. Moreover, the outlet temperature of the fluid and the TES mean temperature are getting closer by increasing the length and becoming almost the same for 1000 m of TES pipe. When the pipe length increases to 2000 m, the outlet temperature of the fluid will be lower than TES mean temperature at different times during the charging, and it remains higher than TES mean temperature during discharging period. Therefore, it can be concluded that the increase in pipe length leads to an increase in charging time (Fig. 6d), and the quality of the energy stored in the TES results from the increment of heat capacity of the TES.

For estimating the maximum heat which can be stored in the TES with 2000 m pipe, the heat transfer rate between the solar system working fluid and the concrete at different times are presented in Fig. 7. As it can be seen in this figure, since the maximum temperature difference is happening in the early hours of the charging process, the maximum heat transfer of approximately 660 kW is achieved at the first timestep. Then, it starts to decrease until the temperature difference between concrete and the fluid is approximately zero, and the TES is fully charged (at 82 h). After that, the discharging time begins, and the heat will be transferred from TES to the solar system working fluid.

The isothermal lines around the pipe in the TES at various radial distances from pipe center are demonstrated in Fig. 8a. As it can be seen in this figure, the temperature difference between isothermal lines decreases by the increase in distance from the pipe center. This confirms

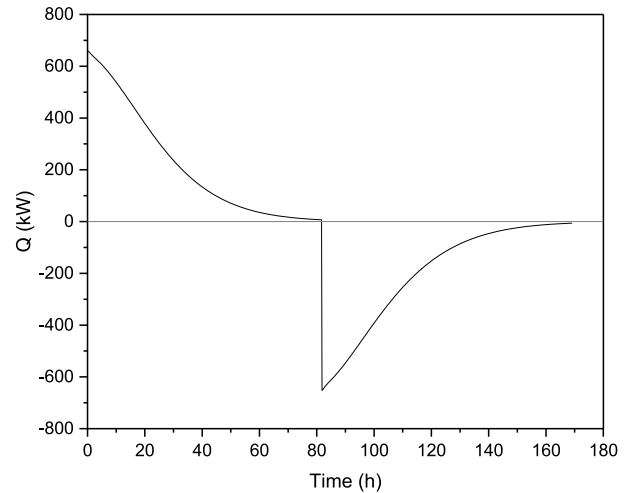


Fig. 7. The TES heat transfer rate during the charging and discharging process in the TES.

that the HTF temperature change reaches the outer layer later than other layers. The solar system working fluid mean temperatures for various longitudinal sections of the TES pipe are also shown in Fig. 8b. There is a significant temperature difference between the inlet (0 m) and the outlet (2000 m) sections of the pipe in the middle of charging time (from 10 h to 30 h). However, by the increase of the TES temperature, the temperature difference between these sections becomes negligible (at 82 h). During the discharging time, it can be seen that there is a significant temperature difference among inlet and outlet sections between 90 h and 130 h. Also, it should be noted that by increasing the length of the TES, the temperature shifts towards the right, which is more stable for the ORC system.

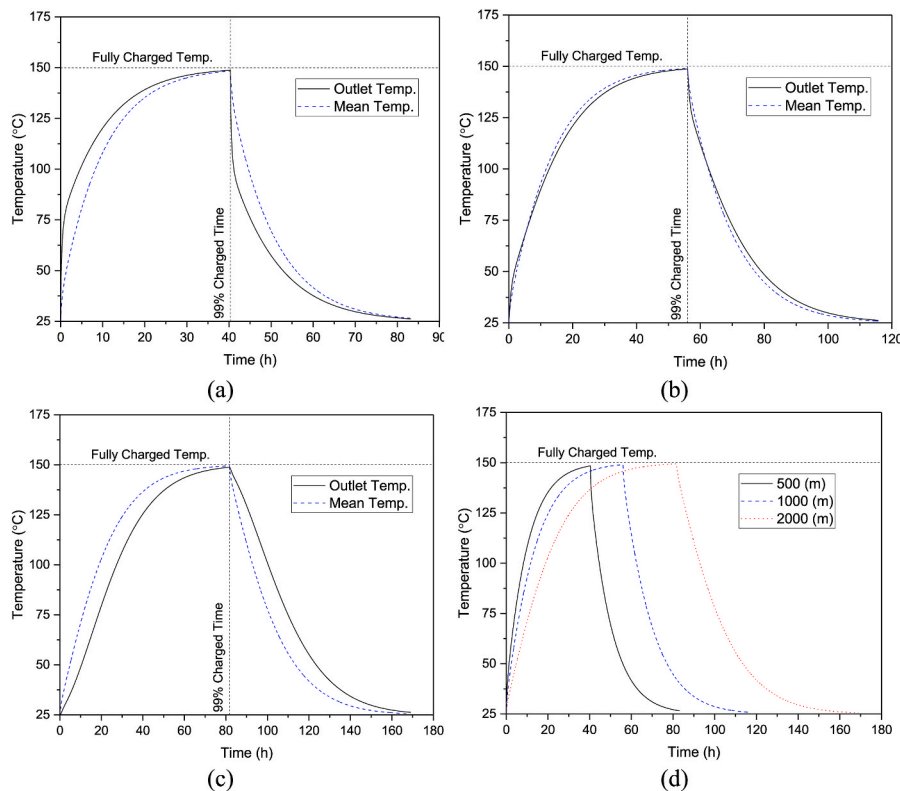


Fig. 6. The TES mean temperature and fluid outlet temperature at various times during the charging and discharging process in the TES when (a) $L = 500$ m and $D_o = 0.4$ m (b) $L = 1000$ m and $D_o = 0.4$ m (c) $L = 2000$ m and $D_o = 0.4$ m (d) all lengths.

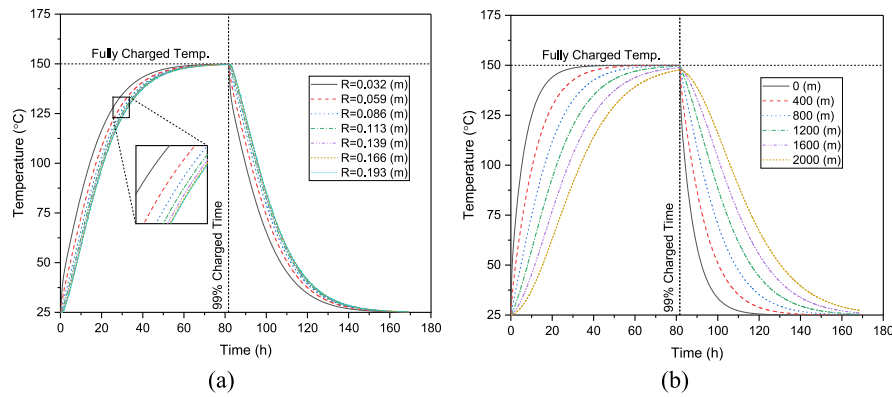


Fig. 8. (a) The isothermal lines around the pipe in the TES in different radial distances from pipe center (b) The mean temperature of the solar thermal system working fluid in different longitudinal sections of TES.

5.2. Whole system parametric analysis

In this section, the impacts of various TES parameters on the performance of the complete system are investigated. Fig. 9a indicates the ORC electrical power generation duration when different TES pipe diameters are used. In this figure, the total length of the pipe and the mass flow ratio of the ratio valve equals 1000 m and 0.75, respectively. By increasing the TES pipe diameter up to 0.4 m, the power generation duration by ORC increases significantly to about 4.5 h. However, by increasing the TES pipe diameter from 0.4 m to 0.6 m, the power generation duration is not changing significantly.

Fig. 9b demonstrates the effects of the TES pipe length parameter on the ORC power generation duration. The results presented in Fig. 9b are for the TES pipe diameter of 0.4 m as the optimum obtained from the Fig. 9a. As it can be clearly seen in this figure, by increasing the TES pipe length from 500 m to 2000 m, the ORC power generation duration increases significantly from 3:38 to 5:22. Additionally, an increase in TES pipe length from 2000 m to 2500 m resulted in a minimal decrease in ORC power generation duration.

The impact of mass flow ratio of the ratio valve (see Fig. 1) on the ORC power generation duration is shown in Fig. 9c. With the mass flow ratio increasing between 0.3 and 1, the ORC power generation duration increased up to 3 h. Therefore, it can be concluded that for achieving the maximum ORC power generation duration, the solar system fluid should flow through TES all the time after leaving the CPCs (See Fig. 1).

Using the analysis provided for Fig. 9 the optimum conditions of TES operation would be inferred which are the TES pipe diameter, length, and mass flow ratio of 0.4 m, 2000 m, and 1, consecutively. Fig. 10 indicates the solar system working fluid temperature variations at the inlet of the heat exchanger (see Fig. 1) and ORC power output during ten days of the system continuous work without and with TES (with the optimum condition), respectively. Each bar chart in Fig. 10 indicates the ORC power generation for the period of 10 min. As it can be seen in Fig. 10a, there are 19 bar charts in Figs. 10a and 38 bar charts in Fig. 10b, the values of which are approximately 100 kW and 50 kW, respectively. In addition, it can be concluded that the ORC generates power for nearly 3.16 h and 6.33 h of the day without and with TES (see Table 1). In addition, the mixture temperature fluctuation is due to the

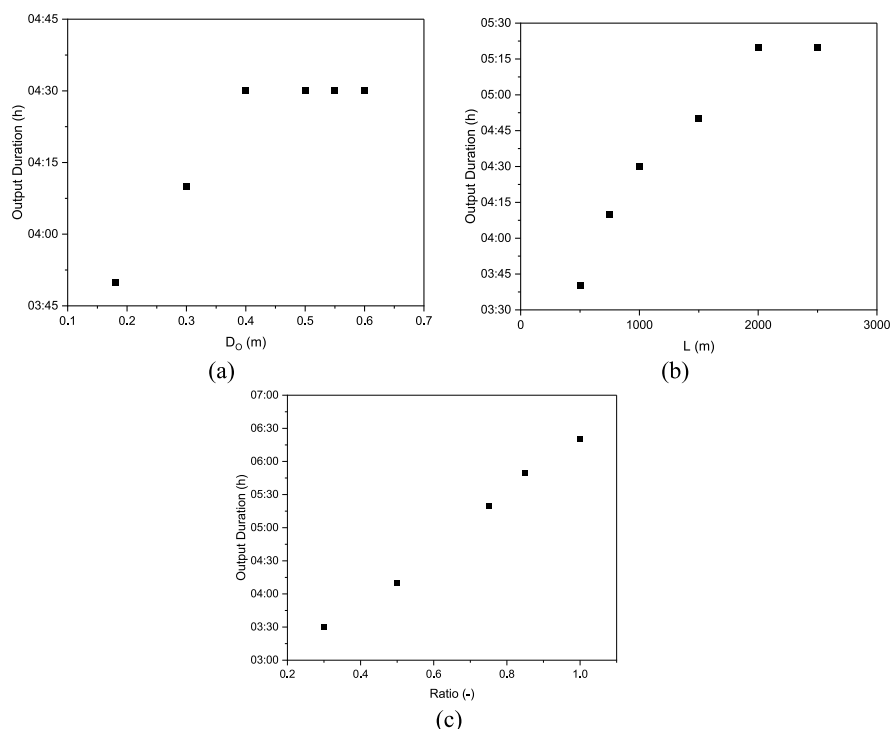


Fig. 9. ORC's daily electrical power generation duration in different (a) TES pipe diameters (b) TES pipe lengths (c) mass flow ratios.

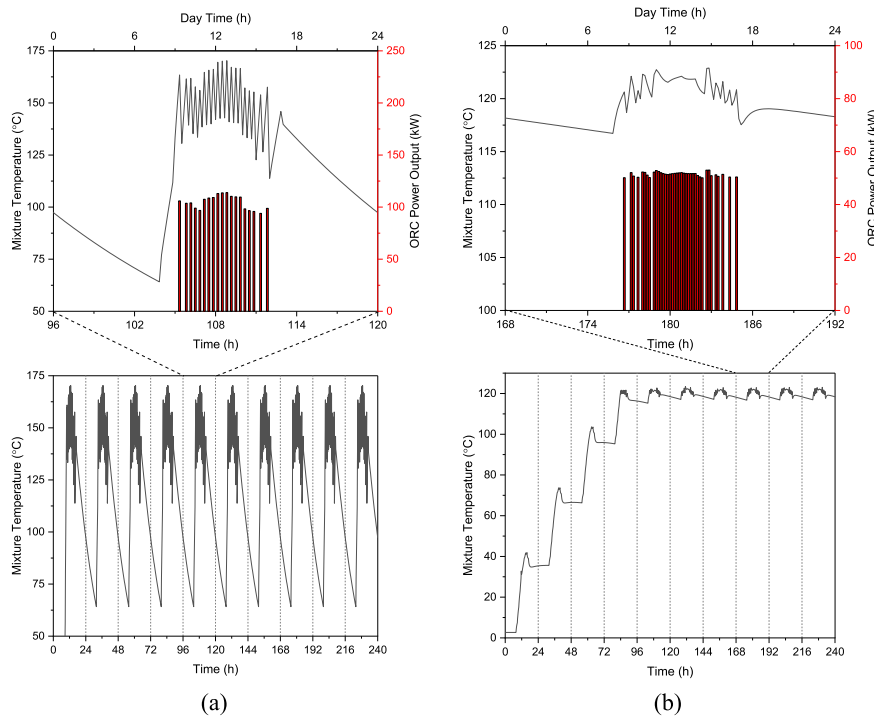


Fig. 10. The solar system working fluid temperature at the inlet of heat exchanger (see Fig. 1) and ORC power output at various times and days when (a) TES is not employed, (b) TES is employed.

Table 1
The system outputs at day 10 with and without TES.

Parameter	Without TES	With TES
ORC power generation rate [kWh]	331.5	327.2
Condenser heat [kWh]	3907.8	3824.2
ORC daily working hour [h]	3:10	6:20

system threshold for starting the ORC power generation unit which is 137 °C. When the system starts, this causes a high temperature drop for about 10 min and the ORC heat exchanger temperature will be 81 °C. The temperature of HTF will increase after passing through the CPC but after mixing with TES outlet, it will not reach to 137 °C and the ORC system will not start till the mixture temperature reach 137 °C which usually takes a 10-min cycle.

Fig. 10b indicates that it takes about three days for TES to be fully charged, and during this period, the electrical power cannot be generated by ORC, as there is no feed to the ORC system because of low temperature during the first 72 h, the temperature will not fluctuate during this period. After this period, the ORC power generation begins as the solar system working fluid reaches its desired temperature. By referring to Tables 1 and it can be inferred that the employment of TES doubles the ORC working hours compared to the system output without TES. Furthermore, the power generation of ORC decreased by 1.3%, and its heat generation increased by 0.49% by using TES. Hence, by adding the TES, the electrical and condenser outputs have not changed significantly, but the hours in which the ORC is working and producing electrical energy have doubled. So this system can ideally extend the hours of operation and make it suitable for use in domestic areas in district heating in which the power is also needed in the afternoon.

The rate of heat and power generated by ORC when integrated with TES and solar system is provided in Fig. 11 at various times during ORC activation days. This figure indicates that nearly 600 kW of heat and 50 kW electrical power are generated continuously during the working hours of the ORC. In addition, the energy flow diagram of the proposed system is presented in Fig. 12. This figure is plotted using the data

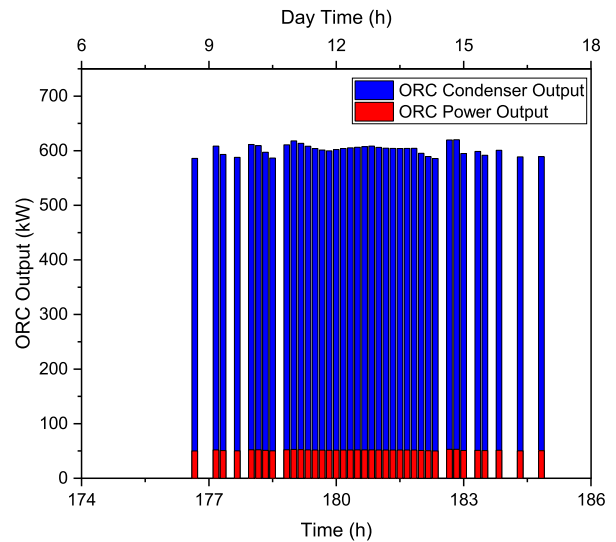


Fig. 11. The ORC heat and power output at various times during ORC activation days.

obtained from the model at the ORC activation days. TES waste is near zero as we assumed it is buried under the ground. However, CPC systems are usually located in an open area, and they are exposed to wind, and open sky. So, we considered these losses in the CPC. Also, the ORC systems could be installed in well controlled indoor space and the only major heat loss would be through the condenser. The total heat dissipation of the CPCs and ORC equals 225.2 kWh and 13.5 kWh, respectively. The CPC system losses include the convective heat transfer of the CPC pipes and the reversed radiation to the peripheral space. Also, most of the energy in the ORC system is transferred to the condenser. This happens because of the relatively low input temperature of the ORC system, which keeps the system’s electrical efficiency lower than 8%.

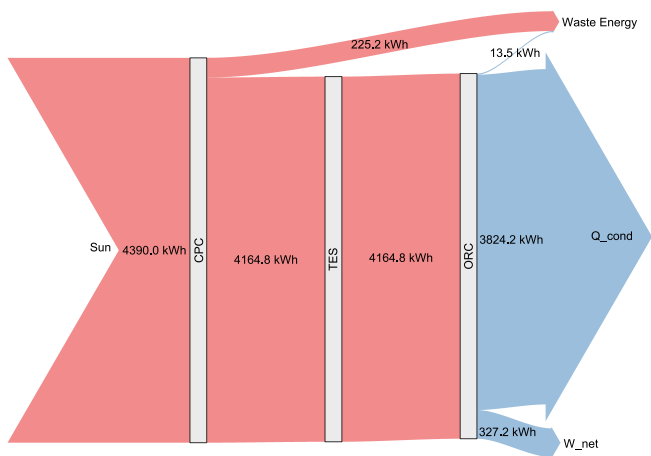


Fig. 12. The energy flow diagram of the proposed system.

The high amount of energy in the ORC condenser makes the system more reliable during the winter because it can provide the energy for space district heating (heating and hot water demand) in the houses.

6. Conclusion

This paper performs a parametric study for integrating concrete TES with a solar-driven ORC system. The proposed system is simulated in MATLAB software, and a detailed parametric study is performed to find the optimum conditions of TES and the complete system. Finally, the whole system with TES in optimum condition is compared to the solar-driven ORC without TES. Since the structure foundation for the thermal collectors in the solar field is usually built of concrete, the proposed concrete bed TES can be embedded in the solar field to reduce capital costs. Furthermore, the low-grade heat stored in concrete bed TES is not affecting the mechanical strength of the foundations.

The main conclusions that can be drawn from this study are as follows:

- By increasing the TES pipe length up to 2000 m, the TES heat storage capacity and duration of the charging time increased significantly to 660 kW and 82 h.
- The maximum ORC working time period (=6:20) is achieved when the TES pipe diameter, length, and three-way valve ratio equal 0.4 m, 2000 m, and 1, respectively. The ratio of one means that the solar system working fluid should flow through TES before the ORC system.
- It takes almost three days for the TES system to be fully charged when it is coupled to a solar-driven ORC. After that, it can produce about 327.2 kWh of electrical power and 3824.2 kWh of heat for district heating purposes.
- The ORC daily working hours doubled from 3:10 h to 6:20 when TES is added to solar-driven ORC. However, the power generation rate of ORC decreased by approximately 1.3%.

CRediT authorship contribution statement

Amin Shakeri: Conceptualization, Methodology, Software, Visualization, Validation, Formal analysis, Investigation, Data curation, Writing – original draft, and Revision. **Hossein Eshghi:** Conceptualization, Methodology, Software, Investigation, Writing – original draft. **Farhad Salek:** Conceptualization, Methodology, Software, Writing – original draft, and Revision. **Meisam Babaie:** Supervision, Conceptualization, Methodology, Writing – review & editing.

Declaration of competing interest

The authors declare that they have no known competing financial interests or personal relationships that could have appeared to influence the work reported in this paper.

Data availability

Data will be made available on request.

Appendix A

The specification of the Compound Parabolic Collector is mentioned in Table A1.

Table A1 Specifications of CPCs

Parameter	Value
Working fluid	Therminol VP-1
Working fluid pressure [bar]	4
Tube length (L) [m]	25
Cover material	Glass
Cover tube emittance (ϵ_c)	0.88
Cover tube outer diameter (D_{co}) [mm]	60
Cover tube inner diameter (D_{ci}) [mm]	58
Receiver material	Stainless steel
Receiver tube emittance (ϵ_r)	0.31
Receivertube outer diameter (D_{ro}) [mm]	40
Receiver tube inner diameter (D_{ri}) [mm]	38
Receiver tube thermal conductivity (k_r) [W/m.K]	16.06
Concentration ratio	3.608
Cover area (A_c) [m ²]	0.0707

The thermophysical properties of Therminol are included in Table A2.

Table A2

Therminol thermophysical properties. The Organic Rankine Cycle working parameters are mentioned in Table A3

Property	Value
Density (ρ) [kg/m ³]	$-0.8343T_m + 1081.6$
Viscosity (μ) [Pa.s]	$0.0044e^{(-0.013 \times T_m)}$
Thermal Capacity (Cp) [J/kg.K]	$2.7955T_m + 1493.1$
Thermal Conductivity (k) [W/m.K]	$-0.0001T_m + 0.1395$

Table A3

ORC constant parameters

Parameter	Value
Working fluid	R245fa
Turbine isentropic efficiency	0.85
Turbine mechanical efficiency	0.98
Pump isentropic efficiency	0.9
High-pressure streams pressure [bar]	15
Low-pressure streams pressure [bar]	5
Electric machine electrical efficiency	0.98
Minimum Working Temperature [K]	400

Appendix B

It is assumed that the proposed system is installed in Shahrood city with parameters indicated in Table B1.

Table B1

The initial conditions of the solar system model

Parameter	Value
Solar field area [m ²]	1000
Geographic latitude	36.4°
Simulation start date (The beginning date of winter in Iran)	21st December
The average ambient temperature [°C]	2.7

References

- [1] F. Salek, M. Zamen, S.V. Hosseini, M. Babaie, Novel hybrid system of pulsed HHO generator/TEG waste heat recovery for CO reduction of a gasoline engine, *Int. J. Hydrogen Energy* 45 (43) (2020) 23576–23586.
- [2] Q. Xiong, S. Altnji, T. Tayebi, M. Izadi, A. Hajjar, B. Sundén, et al., A comprehensive review on the application of hybrid nanofluids in solar energy collectors, *Sustain. Energy Technol. Assessments* 47 (2021), 101341.
- [3] M. Shields, P. Beiter, W. Kleiber, Spatial impacts of technological innovations on the levelized cost of energy for offshore wind power plants in the United States, *Sustain. Energy Technol. Assessments* 45 (2021), 101059.
- [4] O. Arslan, D. Kilic, Concurrent optimization and 4E analysis of organic Rankine cycle power plant driven by parabolic trough collector for low-solar radiation zone, *Sustain. Energy Technol. Assessments* 46 (2021), 101230.
- [5] B. Ghorbani, M. Mehrpooya, M. Sadeqi, Thermodynamic and exergy evaluation of a novel integrated structure for generation and store of power and refrigeration using ammonia-water mixture CCHP cycle and energy storage systems, *Sustain. Energy Technol. Assessments* 47 (2021), 101329.
- [6] O. Calli, C.O. Colpan, H. Gunerhan, Thermo-economic analysis of a biomass and solar energy based organic Rankine cycle system under part load behavior, *Sustain. Energy Technol. Assessments* 46 (2021), 101207.
- [7] A. Kumar, A.K. Tiwari, Z. Said, A comprehensive review analysis on advances of evacuated tube solar collector using nanofluids and PCM, *Sustain. Energy Technol. Assessments* 47 (2021), 101417.
- [8] Y.M.A. Manaserh, A.M. Abubaker, A.D. Ahmad, A.B. Ata, Y.S. Najjar, N.K. Akafuah, Assessment of integrating hybrid solar-combined cycle with thermal energy storage for shaving summer peak load and improving sustainability, *Sustain. Energy Technol. Assessments* 47 (2021), 101505.
- [9] I. Dincer, M. Rosen, *Thermal Energy Storage: Systems and Applications*, John Wiley & Sons, 2002.
- [10] C. Prieto, L.F. Cabeza, Thermal energy storage with phase change materials in solar power plants. Economic analysis, *J. Energy Storage* 43 (2021), 103184.
- [11] E. Guelpa, V. Verda, Thermal energy storage in district heating and cooling systems: a review, *Appl. Energy* 252 (2019), 113474.
- [12] A. Rosato, A. Ciervo, G. Ciampi, M. Scorpio, S. Sibilio, Impact of seasonal thermal energy storage design on the dynamic performance of a solar heating system serving a small-scale Italian district composed of residential and school buildings, *J. Energy Storage* 25 (2019), 100889.
- [13] M. Leško, W. Bujalski, K. Futyma, Operational optimization in district heating systems with the use of thermal energy storage, *Energy* 165 (2018) 902–915.
- [14] Y. Zhang, P. Johansson, A.S. Kalagasidis, Applicability of thermal energy storage in future low-temperature district heating systems – case study using multi-scenario analysis, *Energy Convers. Manag.* 244 (2021), 114518.
- [15] Z. Xi, S. Eshaghi, F. Sardari, Energy, exergy, and exergoeconomic analysis of a polygeneration system driven by solar energy with a thermal energy storage tank for power, heating, and freshwater production, *J. Energy Storage* 36 (2021), 102429.
- [16] S. Rahmadian, H. Rahmanian-Koushaki, P. Omidvar, A. Shahsavari, Nanofluid-PCM heat sink for building integrated concentrated photovoltaic with thermal energy storage and recovery capability, *Sustain. Energy Technol. Assessments* 46 (2021), 101223.
- [17] M.S. Ghoghhaei, A. Mahmoudian, O. Mohammadi, M.B. Shafii, H.J. Mosleh, M. Zandieh, et al., A review on the applications of micro-/nano-encapsulated phase change material slurry in heat transfer and thermal storage systems, *J. Therm. Anal. Calorim.* (2020) 1–24.
- [18] M. Liu, W. Saman, F. Bruno, Review on storage materials and thermal performance enhancement techniques for high temperature phase change thermal storage systems, *Renew. Sustain. Energy Rev.* 16 (4) (2012) 2118–2132.
- [19] G. Mourad, H. Lennox, M. Turner, M. Traynor, Meta-analysis of concrete as a thermal energy storage medium, *PAM Review Energy Science & Technology* 7 (2020).
- [20] H. Li, X. Hao, Q. Qiao, B. Zhang, H. Li, Thermal properties of hybrid fiber-reinforced reactive powder concrete at high temperature, *J. Mater. Civ. Eng.* 32 (3) (2020), 04020022.
- [21] L. Miró, E. Oró, D. Boer, L.F. Cabeza, Embodied energy in thermal energy storage (TES) systems for high temperature applications, *Appl. Energy* 137 (2015) 793–799.

- [22] L. Boquera, J.R. Castro, A.L. Pisello, L.F. Cabeza, Research progress and trends on the use of concrete as thermal energy storage material through bibliometric analysis, *J. Energy Storage* 38 (2021), 102562.
- [23] L. Miró, M.E. Navarro, P. Suresh, A. Gil, A.I. Fernández, L.F. Cabeza, Experimental characterization of a solid industrial by-product as material for high temperature sensible thermal energy storage (TES), *Appl. Energy* 113 (2014) 1261–1268.
- [24] N. Høivik, C. Greiner, J. Barragan, A.C. Iniesta, G. Skeie, P. Bergan, et al., Long-term performance results of concrete-based modular thermal energy storage system, *J. Energy Storage* 24 (2019), 100735.
- [25] D. Mikkelsen, K. Frick, Analysis of controls for integrated energy storage system in energy arbitrage configuration with concrete thermal energy storage, *Appl. Energy* 313 (2022), 118800.
- [26] E. John, M. Hale, P. Selvam, Concrete as a thermal energy storage medium for thermocline solar energy storage systems, *Sol. Energy* 96 (2013) 194–204.
- [27] L. Doretto, F. Martelletto, S. Mancin, Numerical analyses of concrete thermal energy storage systems: effect of the modules' arrangement, *Energy Rep.* 6 (2020) 199–214.
- [28] K. Vigneshwaran, G. Singh Sodhi, P. Muthukumar, S. Subbiah, Concrete Based High Temperature Thermal Energy Storage System: Experimental and Numerical Studies, 198, *Energy Conversion and Management*, 2019, 111905.
- [29] C. Liu, H. Yang, Multi-objective optimization of a concrete thermal energy storage system based on response surface methodology, *Appl. Therm. Eng.* 202 (2022), 117847.
- [30] F. Salek, A.N. Moghaddam, M.M. Naserian, Thermodynamic analysis of diesel engine coupled with ORC and absorption refrigeration cycle, *Energy Convers. Manag.* 140 (2017) 240–246.
- [31] F. Salek, A.N. Moghaddam, M.M. Naserian, Thermodynamic analysis and improvement of a novel solar driven atmospheric water generator, *Energy Convers. Manag.* 161 (2018) 104–111.
- [32] J.A. Duffie, W.A. Beckman, *Solar Engineering of Thermal Processes*, Wiley, 2013.
- [33] T.L. Bergman, F.P. Incropera, D.P. DeWitt, A.S. Lavine, *Fundamentals of Heat and Mass Transfer*, John Wiley & Sons, 2011.
- [34] V. Gnielinski, On heat transfer in tubes, *Int. J. Heat Mass Tran.* 63 (2013) 134–140.
- [35] B. Petukhov, Heat transfer and friction in turbulent pipe flow with variable physical properties, *Elsevier, Adv. Heat Tran.* 6 (1970) 503–564.